

# Impacts of Decoder Latency on Utility-Scale Quantum Computer Architectures

Abdullah Khalid,<sup>1</sup> Allyson Silva,<sup>1</sup> Gebremedhin A. Dagnew,<sup>1,2,3</sup> Tom Dvir,<sup>4</sup> Oded Wertheim,<sup>4</sup> Motty Gruda,<sup>4</sup> Xiangzhou Kong,<sup>1</sup> Mia Kramer,<sup>1</sup> Zak Webb,<sup>1</sup> Artur Scherer,<sup>1</sup> Masoud Mohseni,<sup>5,6</sup> Yonatan Cohen,<sup>4</sup> and Pooya Ronagh<sup>1,2,3,7,\*</sup>

<sup>1</sup>*1QB Information Technologies (1QBit), Vancouver, BC, Canada*

<sup>2</sup>*Department of Physics & Astronomy, University of Waterloo, Waterloo, ON, Canada*

<sup>3</sup>*Perimeter Institute for Theoretical Physics, Waterloo, ON, Canada*

<sup>4</sup>*Quantum Machines, Israel*

<sup>5</sup>*HPE Quantum, Hewlett Packard Labs, CA, USA*

<sup>6</sup>*Emergent Machine Intelligence, Hewlett Packard Labs, CA, USA*

<sup>7</sup>*Institute for Quantum Computing, University of Waterloo, Waterloo, ON, Canada*

(Dated: November 13, 2025)

The speed of a fault-tolerant quantum computer is dictated by the reaction time of its classical electronics, that is, the total time required by decoders and controllers to determine the outcome of a logical measurement and execute subsequent conditional logical operations. Despite its importance, the reaction time and its impact on the design of the logical microarchitecture of a quantum computer are not well understood. In this work, we build, for a surface code based architecture, a model for the reaction time in which the decoder latency is based on parallel space- and time-window decoding methods, and communication latencies are drawn from our envisioned quantum execution environment comprising a high-speed network of quantum processing units, controllers, decoders, and high-performance computing nodes. We use this model to estimate the increase in the logical error rate of magic state injections as a function of the reaction time. Next, we show how the logical microarchitecture can be optimized with respect to the reaction time, and then present detailed full-system quantum and classical resource estimates for executing utility-scale quantum circuits based on realistic hardware noise parameters and state-of-the-art decoding times. For circuits with  $10^6$ – $10^{11}$   $T$  gates involving 200–2000 logical qubits, under a  $\Lambda = 9.3$  hardware model representative of a realistic target for superconducting quantum processors operating at a 2.86 MHz stabilization frequency, we show that even decoding at a sub-microsecond per stabilization round speed introduces substantial resource overheads: approximately 100k–250k additional physical qubits for correction qubit storage in the magic state factory; 300k–1.75M extra physical qubits in the core processor due to the code distance increase of  $d$  to  $d + 4$  for extra memory protection; and a longer runtime by roughly a factor of 100.

## I. INTRODUCTION

Fault-tolerant quantum computation (FTQC) is an inherently hybrid quantum–classical scheme that involves executing quantum circuits, measuring subsets of the qubits involved in the circuits yielding error syndromes, classically inferring the most probable errors from the syndromes, and repeating this process iteratively. Utility-scale quantum programs require performing trillions of operations on thousands of logical qubits [1]. Therefore, their corresponding fault-tolerantly compiled physical circuits require millions of qubits to operate robustly in communication with classical control and decoding electronics for many hours, days, or even longer. Building such a complex machine presents many systems-engineering challenges. In this paper, we focus on the challenges caused by the delays produced by this hybrid process and discuss how system and software architectures can be adapted to minimize the impact of these delays in the performance of a quantum computer.

\* Corresponding author: pooya.ronagh@1qbit.com

Indeed, *reaction time*, that is, the sum of the decoder latency and the control electronics latency [2], determines the speed of a quantum computer. Minimizing the reaction time is crucial for fast qubits (superconducting, topological, spin, etc.); otherwise, the low gate and measurement times of these qubits are overshadowed by slow decoders. In a recent study [3], we discuss how the (logical) *microarchitecture* of surface code based quantum processing units (QPU) can be optimized with respect to the reaction time. A microarchitecture is an abstract partitioning of a QPU into dedicated areas for various fault-tolerant procedures, and is crucial for creating the appropriate abstraction layers within the compilation stack of the computer.

In this work, we extend our analysis of the impact of reaction time on the software and system architecture of a quantum computer in multiple novel ways. First, we identify the two reaction times in our microarchitecture, but determine, based on a method that combines parallel space- and time-window decoding techniques [4, 5], that only one of them controls the speed of the computation. Second, we build a model for the additional logical error accumulated due to the wait induced by the reaction time, and use this model to estimate the required physical qubit count as a function of reaction time for two utility-scale quantum algorithms. Third, we develop decoder latency models for decoding quantum memories and lattice surgeries. We also experimentally measure the communication latencies in our envisioned *quantum execution environment*. The execution environment is a network between the controller, a high-performance decoder cluster, and a *orchestrator* that triggers the execution of quantum applications (see Fig. 2 below). These latencies allow us to achieve realistic estimates of the reaction times and use them to identify the communication channel bandwidths and multiplicities required between classical processors to construct a seamless quantum execution environment. Moreover, we identify target performance metrics for decoders that enable achieving quantum circuit execution times within a threshold ranging from an hour to a month. Finally, we estimate the number of decoding units required for throughput-matched decoding of a quantum circuit.

The paper is organized as follows. In Section II we review background work on surface codes and their decoding, fault-tolerant quantum compilation and assembly, and optimization of logical microarchitectures. In Section III, we describe our envisioned quantum execution environment for a quantum computer, highlighting the flow of instructions and information between the classical and quantum processing units. Here, we also present experimentally determined numbers for the communication latency between different units. In Section IV, we analyze the reaction time for a magic state injection protocol and the resulting decoding jobs required to be completed at runtime. We provide our main results in Sections V and VI. In Section V, we show the impact of reaction time on optimal microarchitectures and physical qubit counts. We identify decoder speed requirements and the number of decoders necessary for utility-scale quantum computing in Section VI. Finally, we provide our concluding remarks in Section VII.

## II. BACKGROUND

### A. FTQC Computation with Surface Codes

In this paper, we study fault-tolerant architectures based on the rotated surface code [6–8]. In the simplest case, a  $d \times d$  square patch of data qubits can be used encode a single logical qubit with an error-correcting distance of  $d$ . However, others shapes and configurations are possible, for example, one can also encode two logical qubits in a  $2d \times d$  patch of data qubits with distance  $d$  [7, 9, 10]. Sections of the geometric boundaries of these patches define the logical Pauli operators of the qubits.

A variety of operations are possible on the surface code patches laid out in a 2D geometry [11].

Single-qubit Pauli operations and their measurement can be performed by directly acting on the data qubits. Single-qubit patches may also be grown into large patches using the growth protocol. Multi-qubit operations, however, are performed using *lattice surgery*, in which interactions between code patches are engineered by merging them and then splitting them back into distinct patches [8, 9, 12, 13]. This results in a joint measurement of the patches in the basis of the Pauli operators associated with the merged boundaries of the patches. For example, if the  $X$  boundaries of two patches in the logical  $|00\rangle_L$  state are merged and split, the qubits are prepared in the Bell state

$$\frac{1}{\sqrt{2}}(I + (-1)^m X_{L,0} X_{L,1})|00\rangle_L = \frac{1}{\sqrt{2}}(|00\rangle_L + (-1)^m |11\rangle_L), \quad (1)$$

where  $m \in \{0, 1\}$  is the outcome of the measurement, determined by multiplying the value of all  $X$  syndromes in the bus region connecting the two patches. This is called an  $XX$  surgery.

These multi-qubit Pauli measurements along with ancilla prepared in specific states can be used to engineer more interesting multi-qubit operations, such as rotations by  $\theta = \pi/4$  or  $\pi/8$  around the axis of  $P$ , that is, the interaction  $|\psi\rangle \rightarrow e^{i\theta P}|\psi\rangle$  [10]. The non-Clifford  $\pi/8$  rotation gadget is particularly important, because a quantum algorithm can be compiled into a sequence consisting merely of multi-qubit  $\pi/8$ -th rotations. An implementation of the post-corrected  $\pi/8$  rotation gadget from Ref. [10] is shown in Fig. 3. In this gadget,  $P$  is the multi-qubit Pauli operator specifying the generator for the multi-qubit rotation to be applied to the joint quantum state of participating logical data qubits. First, a magic state  $|m\rangle$  is entangled with a *correction qubit* initialized in  $|0\rangle$  using a  $Z \otimes Y$  lattice surgery. Then, a  $P \otimes Z$  surgery is used to entangle the magic state qubit with the computational data qubits initially in the state  $|\psi\rangle$ . Finally, the magic state qubit is measured in the  $X$  basis. To ensure that the correct rotation has been implemented requires an additional step. The correction qubit must be measured in either the  $X$  or the  $Z$  basis, where the choice depends on the lattice surgery measurement outcomes and the magic state qubit measurement. It also depends on the measurement outcomes of correction qubits in preceding  $\pi/8$  rotations that anti-commute with  $P$ . The role of the decoder and control electronics as it relates to this conditional measurement is discussed in explicit detail in Section VI A.

## B. Optimizing the Fault-Tolerant Microarchitecture

The logical microarchitecture considered in this work builds upon the modular fault-tolerant design introduced in Ref. [3] comprising two main modules: a core processor, where the logical computation is executed, and a multi-level magic state factory (MSF) that continuously produces high-fidelity magic  $T$  states required for the non-Clifford  $\pi/8$  rotations (see Fig. 1). Here, a single core processor is coupled to a multi-level MSF via a quantum bus that transports distilled magic states from the factory to the correction zone, which is a region used to perform the measurements in the  $\pi/8$  rotation gadget that prepare the correction qubit using a magic state before this magic state is consumed in the core. Each zone is composed of surface code patches arranged in a planar layout comprising distinct functions. The patches and their functions are: *magic state preparation* patches create logical magic states; *magic state storage* and *code growth* patches buffer and enlarge them, respectively; *Distillation Unit (DU)* *data qubit* and *output* patches hold the data required to implement the distillation; *correction qubit preparation* and *correction qubit storage* patches support the post-corrected  $\pi/8$  protocol and keeps the entangled correction qubit around until the classical processing provides the instructions on how to measure it; and *computational qubit* patches store the algorithm's logical qubits. This modular configuration of the architecture with the preparation, distillation and correction protocols performed in dedicated units allows the (magic states and correction qubits) resource flows to be resized by simply defining the number and size of the structures required by them.

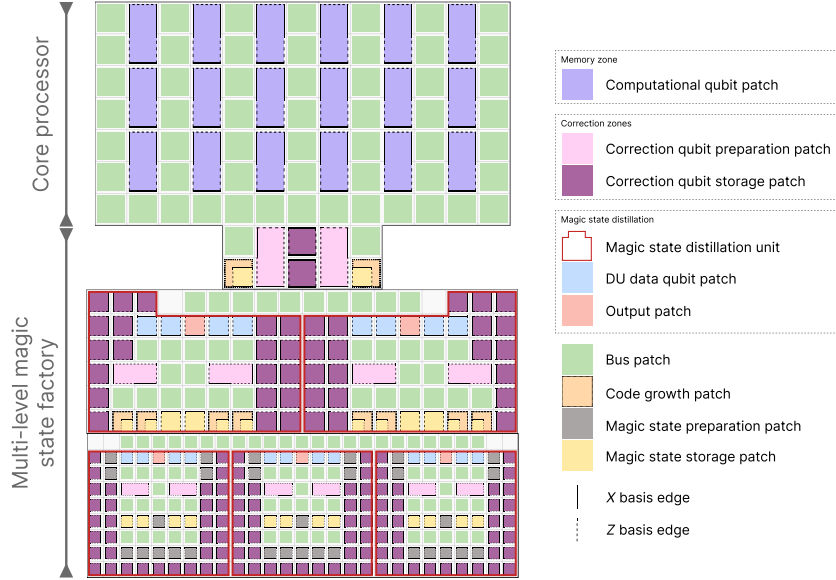


FIG. 1: Target logical microarchitecture with a core processor sized for an algorithm requiring 36 logical qubits, coupled to an MSF with two distillation levels, each containing parallel (three lower-level and two higher-level) distillation units designed to implement the 15-to-1 magic state distillation protocol [10]. Dedicated regions (the correction areas) are allocated for preparing and storing the correction qubits required for the post-corrected  $\pi/8$  rotation gadget. The number of correction qubit storage patches required per distillation unit is determined by the reaction time expressed in logical cycles, i.e.,  $\lceil \gamma_{\text{mem}} / \tau_{\text{logical}} \rceil$ , where the logical cycle time  $\tau_{\text{logical}}$  is set by the code distance used in the corresponding distillation unit. Our assembly onto this microarchitecture determines the code distances for the logical patches, which can be different for each distillation level and for the core processor; the number of parallel distillation units required to achieve just-in-time resource delivery while accounting for classical decoding latency; and the storage capacity required for correction buffers. Further details are provided in Ref. [3].

The assembly of the quantum circuit in this architecture is done by first allocating a total logical error budget across the components that contribute logical errors along the execution path. The error contributions we consider are: (i) memory errors on idling computational and storage qubits; (ii) lattice surgery errors during multi-qubit measurements; and (iii) MSF-induced errors, comprising preparation infidelity, logical faults within distillation rounds, and inter-level code growth and magic state transport. These contributions accumulate approximately additively over the sequence of logical events in a compiled schedule. Thus, meeting the error budget requires choosing code distances and capacities (e.g., number of parallel distillation units in each level) such that the sum of logical error contributions remains below the error budget.

Within this feasible region, optimal microarchitectures are those that minimize the space and/or time overhead. The time-optimal design is achieved when the MSF produces magic states at the same rate that the core can consume them. Faster decoders reduce the time spent waiting on instructions for the correction qubit and therefore allow higher consumption rates. Even with decoder responses faster than logical cycle times, reaction time is the limiting factor in the post-corrected model since non-commuting  $T$  gates can be parallelized via quantum teleportation [14]. Space-optimal designs deliberately create undersized MSFs to trade runtime for fewer logical qubits. However, if undersized too aggressively, idling grows, memory error increases, and higher code distances may be required to stay within the budget, which may lead to a higher space overhead

instead.

Decoder latency directly affects this balance. Each correction qubit produced by the  $\pi/8$  gadget must remain stored until the controller returns the instructions for the measurement basis for that qubit, determined from the outcomes of its dependent measurements. As soon as a correction qubit is measured, its storage patch is released and can be reused.

For distillation protocols where all  $\pi/8$  rotations are commutable (e.g., the 15-to-1 protocol), the decision on the basis of each correction qubit measurement depends only on measurement outcomes within its own  $\pi/8$  gadget. There are no cross-gadget dependencies. Consequently, when a correction qubit is prepared, it must be held in storage until the decoder processes the last dependent measurement for that gadget. In steady state, this creates a pipeline in which a correction qubit enters storage roughly every logical cycle and remains stored for  $\lceil \gamma_{\text{mem}} / \tau_{\text{logical}} \rceil$  logical cycles, which represents the reaction time  $\gamma_{\text{mem}}$  expressed in logical cycles  $\tau_{\text{logical}}$  (see IV for more details). With sufficient decoder parallelism, the peak number of concurrently idling qubits per distillation unit is therefore exactly this ratio. Thus, each unit must provision at least this number of correction storage patches to avoid stalls due to insufficient storage.

Since classical decoding can delay the consumption of correction qubits, the effective throughput of the distillation pipeline is constrained not only by the protocol rate, but also by the reaction time. Consequently, the MSF size (number of parallel distillation units per level) should be tuned to deliver magic states in a just-in-time manner rather than blindly increasing the production capacity. This yields high utilization of resources while avoiding unnecessary space overhead.

### C. Performance of FTQC Operations

The optimal size and number of different modules in the FTQC architecture, as well as the code distance at which they operate can be determined using the predicted performance of logical surface code operations on a given QPU, which is specified through the noise affecting its qubits and gates. For our simulations, we employ a circuit-level depolarizing noise model that is characterized by 11 parameters that determine one- and two-qubit gate errors, state preparation and measurement errors, and idling errors [1]. These parameters and the values we use are shown in Table I. Note that this parameter set implies that a stabilizer measurement round is only  $0.35 \mu\text{s}$ . This does not include the time taken for error suppression techniques like dynamic decoupling or leakage removal, which need to be employed on realistic quantum processors [15, 16], and result in stabilizer round time of  $\sim 1 \mu\text{s}$ .

Using this noise model and its parameter values, we characterize the four fundamental logical operations used in our FTQC architecture: quantum memory, growth, magic state preparation and lattice surgery [11]. Each operation acts on one or more patches of size  $d \times d$  and takes exactly  $d$  stabilization rounds, and hence a logical cycle time of  $\tau_{\text{logical}} = d \mu\text{s}$ . This ensures synchronization of all operations in a single module in our microarchitecture. As reported previously [1], under the chosen noise model, the logical error rate of quantum memory is

$$P_{\text{mem}}(d) = \mu \times d^2 \times \Lambda^{-\frac{d+1}{2}}, \quad (2)$$

where  $\mu = 0.019(4)$  and  $\Lambda = 9.3(3)$ . Due to the similarity in the protocols, we approximate the error rate of the growth protocol by the quantum memory protocol. We selected magic state cultivation as the magic state preparation protocol due to its impressive performance [17]. This is a non-deterministic protocol, whose logical error rate for distances  $d \leq 25$  is  $P_{\text{magic}} \leq 4.73 \times 10^{-5}$  and discard rate is 0.41 [1]. The performance of lattice surgery is presented in Section V.

Hardware Parameter	Value
$T_1, T_2$ times	200 $\mu$ s
Single-qubit gate error	0.0002
Two-qubit gate error	0.0005
State preparation error	0.01
Measurement error	0.005
Reset error	0.005
Single-qubit gate time	25 ns
Two-qubit gate time	25 ns
State preparation time	1 $\mu$ s
Measurement time	100 ns
Reset time	100 ns

TABLE I: Target hardware specifications for gate error rates and times, and qubit relaxation and coherence times, which are believed to be achievable in the near term for superconducting quantum processors. This hardware parameter set serves as the input to the circuit-level depolarizing noise model presented in Ref. [1].

#### D. Decoding Surface Codes

Due to their attractive error correcting property and relative simplicity to implementation, many decoders have been developed for the surface code (see Refs. [18, 19] for recent reviews). These decoders can be judged upon three key metrics: accuracy, throughput and latency. The *accuracy* of a decoder characterizes its ability to identify errors. The *throughput* is the rate at which a decoder processes syndromes. If this is less than the rate at which syndromes are produced, the quantum computation will slow down exponentially [20]. The *latency* is the time between the events when syndromes are made available to a decoder, and when it outputs a result.

While surface code decoders have very low logical error rates, they struggle to match the throughput of the syndrome data produced, especially on superconducting qubit-based QPUs where the stabilization round time is 1  $\mu$ s. The state-of-the-art decoder for surface codes is an FPGA implementation of the Union-Find decoder [21, 22] by Riverlane, which has a decoding time per stabilization round of 1.0  $\mu$ s for a  $d = 30$  quantum memory [23]. Such a decoder is fast enough to decode a  $d \leq 30$  quantum memory, if the stabilization time on the QPU is equal to or greater than 1.0  $\mu$ s. However, lattice surgeries used in our FTQC architecture can involve hundreds or even thousands of patches, which require correspondingly larger throughputs from the decoder. The latency of decoding such lattice surgeries using single decoding units would be practically unfeasible for utility-scale quantum computing.

Fortunately, various methods have been developed recently to break up a single decoding task into several smaller tasks that can then be solved in parallel on the classical coprocessor [4, 5, 24–27]. These methods can significantly reduce the throughput requirements of a single decoder unit, as well as reduce the total latency of the decoding task, at the cost of more decoding units. In this work, we use two such parallelization algorithms to build decoder latency models [4, 5]. These algorithms break the decoding graph [13, 28–31], into overlapping regions called windows, that are then decoded separately and their results combined.

The decoding task of a single distance  $d$  surface code patch stored in memory for many logical cycles can be solved by employing a strategy based on parallel windows in time [5]. Sub-decoding tasks decode windows that have any spatial size and  $3d$  temporal size, and belong to one of two layers, called layers  $A$  and  $B$ . In layer  $A$  the windows associated with different tasks are separated by a gap of  $d$  rounds (called the gap region). The window for each task has three  $d$ -sized sub-regions: a buffer region, a commit region, and another buffer region. Once a layer  $A$  decoding task

is complete, the corrections in the commit region are preserved, while the error strings extending from the commit region to the buffer regions are used to create artificial defects at the boundaries of the buffer regions. In layer  $B$ , decoding tasks solve decoding graphs of size  $3d$  as well, where each decoding graph consists of the two buffer regions and the gap region between two commit regions from layer  $A$ . Hence, a layer  $B$  task can be solved once the two adjacent layer  $A$  tasks have been solved. All tasks in a single layer can, in principle, be decoded in parallel. Hence, in the absence of parallelization overhead, if a single window is decoded in time  $\tau_w$ , then the decoder latency is  $2\tau_w$ .

Decoding a lattice surgery between many different patches instead requires parallel windows in the space dimensions of the decoding graph [4]. Here, the number of layers is two, if the lattice surgery Pauli operator consists only of  $X$  and  $Z$  operators, and the number of layers is three if the Pauli operator has at least one  $Y$  term. The windows in this method also contain commit and buffer region. The key ideas to ensure high accuracy is that windows in a single layer must not overlap their commit regions, and these commit regions must have spatial size  $d \times d$ . In the  $Y$  surgery case, the first layer windows have  $d/2$ -sized buffers on all sides of the commit region, which results in windows of size  $2d \times 2d$ . The windows in the second layer have size  $2d \times 1.5d$ , because some of the decoding graph has already been committed. Finally, the third-layer windows consist of only commit regions of size  $d \times d$ . All windows have temporal size  $d$  because they are decoding a single logical operation.

### III. THE QUANTUM EXECUTION ENVIRONMENT

In this section, we describe our envisioned quantum execution environment, as shown in Fig. 2. The execution environment is a multi-channel architecture in which a modular controller communicates with a modular decoder stack and an orchestrator. The setup supports up to 1000 parallel communication channels, enabling concurrent data transfer and processing across system layers.

The orchestrator is a classical computing device that serves as the execution provider. It receives a quantum program that has been compiled to surgeries with designated surface code patches involved as described in Section II B. We call this the *surgery intermediate representation* language, or surgery IR for short. The orchestrator parses the quantum program provided in surgery IR into a compact representation of the physical stabilizer circuits which we call the *physical IR*. This data transfer is performed at the  $t_{oc}$  rate as shown in Fig. 2 and Table II. The physical IR contains a large amount of data. For a QPU with 10 million qubits, the total bandwidths of the links is in the Tb/s regime, which is well within existing networking technology, given the right divisions of this bandwidth in the orchestrator-controller-QPU links.

The orchestrator also determines the decoding windows for each surgery and the sequence of all decoding jobs required for decoding each surgery with their dependencies as explained in Section II D. This information is communicated directly to the decoder cluster ahead of time and therefore it does not contribute to the reaction time. We assume that the decoder cluster is equipped with an efficient workload manager that queues the decoding jobs and communicates dependencies between them. The dependencies are the boundaries of committed decoding regions from prior decoding windows and therefore is a small number of bits (90 bits for distance 30 as per Ref. [4]) to be communicated in time  $t_{dd}$ .

After the execution of a stabilization cycle (parity-check circuit), the syndrome qubits are measured and the results are transmitted from the controller to the decoder cluster. Thanks to throughput improvements from decoding parallelization the total RAM required for storing syndrome measurement outcomes is on the order of gigabytes, as discussed in Section VI B.

When the decoding of a surgery is complete, the results are transmitted to the orchestrator.

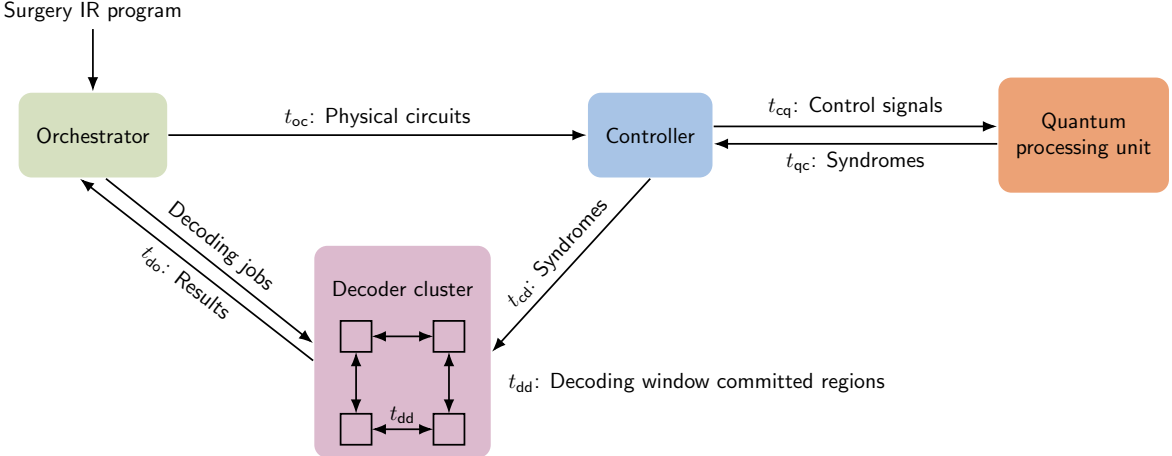


FIG. 2: Schematic of the functional decomposition of the quantum execution environment. Arrows indicate the data transfer directions, and are labelled by the type of data and/or the corresponding communication times.

The orchestrator stores the physical and logical Pauli frames. The decoding results are used to update these frames, and determine the results of logical measurements. The subsequent logical operations that are conditional on these logical measurements are now updated by the orchestrator before they are parsed into physical IR.

### A. Data Transfer Time Measurements

To obtain realistic estimates for the overall reaction time in a future fault-tolerant quantum computer, we decompose it into its constituent subprocesses and benchmark each against available state-of-the-art hardware, extrapolating to a prospective modular architecture. The duration of each subprocess depends critically on the volume of data transferred, the bandwidth of the corresponding communication channels, and the degree of parallelism (i.e., the number of concurrent channels) employed.

The principal subprocesses include the transmission of syndrome data from the QPU to the controller and the return of pulse sequences from the controller to the QPU, both occurring over multiple analog channels and limited primarily by the signal time-of-flight. In addition, the transfer of syndromes to the decoder cluster requires dedicated digital communication links between the controller and the decoders.

In a modular control stack, each control cluster is assumed to manage on the order of  $10^4$  physical qubits and to maintain independent communication links to both the decoder cluster and the orchestrator. This configuration determines the amount of data transmitted from the controller to the decoders in each stabilization round. Consequently, a  $10M$ -qubit computer would consist of roughly  $10^3$  such control-decoder-orchestrator communication channels operating in parallel.

After the completion of decoding and instruction-parsing tasks at the end of every logical cycle the updated control instructions are returned to the controller through the same number of parallel channels. Data exchange within the decoder cluster and between the decoders and orchestrator, supported by high-performance-computing infrastructure, can be highly parallelized and is expected to achieve sub-microsecond latencies per transaction.

We measured the round-trip latencies between an OPX1000 controller and an NVIDIA Grace Hopper server using an OPNIC PCIe-optical interface. The measurements were performed as a

Communication Step	Time [μs]	Size per Channel	Number of Channels
$t_{qc}$ – Syndrome transfer from QPU to controller	0.15	1	$5 \times 10^6$
$t_{cd}$ – Syndrome transfer from controller to decoders	2	5000	1000
$t_{dd}$ – Decoder to decoder exchange	0.5	100	multiple
$t_{do}$ – Decoding results transfer from decoders to orchestrator	1	50,000	100
$t_{oc}$ – Instructions from orchestrator to controller	4	20,000	1000
$t_{cq}$ – Instructions from controller to QPU	0.15	1	$5 \times 10^6$

TABLE II: For the quantum execution environment, the data transfer steps and their associated latency, data size per channel, and number of channels.

function of the data volume transmitted in each direction. We utilize the controller state discrimination capabilities to reduce the required bandwidth to 1–2 bits per qubit. We observe a total communication time of under 2 μs for sending and receiving 1000 bits of data—equivalent to a single logical patch or 3–4 μs for a 10-patch surgery. We note that as the system scales, the interface will be optimized accordingly, with higher channel counts and data rates. Sending the data only to the relevant decoder in the cluster will minimize the latency impact for large data transmission.

To analyze the total reaction time, we decompose it into its constituent smaller steps and estimate the duration of each step. Table II summarizes the estimated time per step in the process. The values reflect the approximate duration per channel, representative data size, and operational periodicity.

Note that the steps preceding the decoding task are executed once per syndrome-extraction round, whereas the steps following decoding are executed once per decoding cycle, that is, approximately every  $d$  syndrome rounds. Using the communication figures above and assuming a multi-channel architecture (up to  $10^3$  parallel channels), the end-to-end communication time from the last measurement to the arrival of updated instructions at the QPU is

$$\tau_{\text{com}} \approx t_{qc} + t_{cd} + t_{dd} + t_{do} + t_{oc} + t_{cq} = \mathcal{O}(10 \mu\text{s}). \quad (3)$$

This budget is dominated by controller-decoder-orchestrator data movement ( $t_{cd}, t_{do}, t_{oc}$ ), whose effective latency scales roughly as  $O(N_S/N_{\text{ch}})$  with payload size  $N_S$  and the available parallelism  $N_{\text{ch}}$ . Because  $N_{\text{ch}}$  and link bandwidth are systems-engineering choices, they can be further optimized (e.g., widening channelization, batching, and overlapping transfers) in light of these measurements to satisfy the latency requirements of efficient FTQC.

#### IV. REACTION TIME IN FTQC

In this section, we discuss why the reaction time determines the overall speed of computation in our fault-tolerant microarchitecture. We present a method combining the spatial- and temporal-window techniques [4, 5] to enable additional decoder parallelization that speeds up the computation. Our analysis continues on from Section II A, where it was explained that the  $\pi/8$  gadget has one conditional operation—the measurement of the correction qubit in either the  $X$ - or the  $Z$ -basis. This decision is based on the outcome of the lattice surgery measurement outcomes

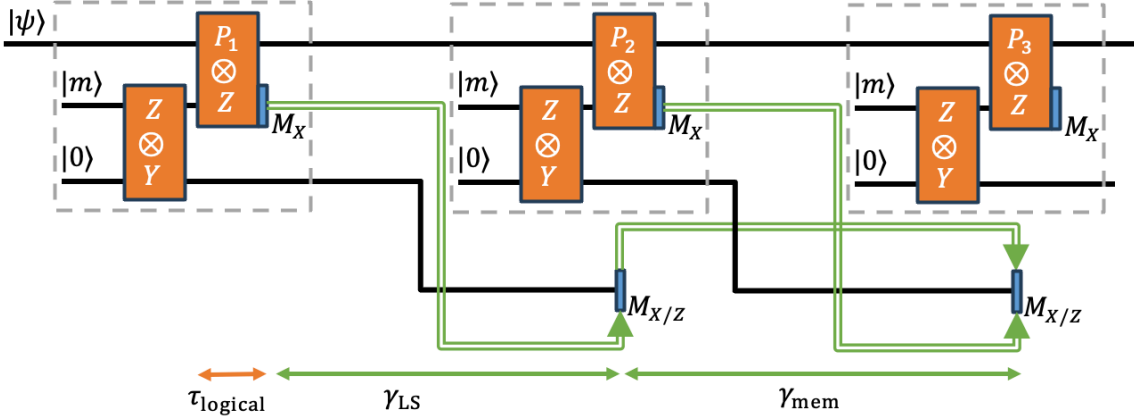


FIG. 3: Implementation of a sequence of post-corrected  $\pi/8$  Pauli rotations on a QPU. Each  $\pi/8$  rotation gadget (indicated by a grey dashed line box) requires performing measurements involving logical data qubits in the joint state  $|\psi\rangle$ , a high-fidelity magic state  $|m\rangle$  distilled in an MSF (not shown), and a correction qubit prepared in the state  $|0\rangle$ . The correction qubit in each rotation gadget is measured in either the  $X$ - or  $Z$ -basis, depending on the outcome of the logical measurements and on the outcome of the measurement of the previous correction qubit. In the classical processor (not shown), the received syndrome data is used to decode the outcomes of the measurements. The lattice surgery measurements involved in implementing each  $\pi/8$  rotation are spatially large and have a reaction time of  $\gamma_{\text{LS}}$ . The correction qubits cannot be measured until their associated lattice surgery measurements have been decoded, so they are stored in memory. Hence, the decoding of each correction qubit measurement has a reaction time of  $\gamma_{\text{mem}}$ . The decoding of the logical measurements can be parallelized, but the decoding of the correction qubit measurements cannot.

in the same  $\pi/8$  gadget, as well as on the measurement outcome of the correction qubit in the previous gadget if the two gadgets anti-commute. It can be assumed that in the core processor all pairs of  $\pi/8$  gadgets anti-commute, which is reasonable if the algorithm has been compiled efficiently. However, in the 15-to-1 magic state distillation protocol, all rotations are  $Z$ -type, and therefore commute with each other [10].

On a noisy device, the correct value of the measurements is discovered once the decoder identifies all errors using the syndrome data. The time it takes to send the syndromes of the two lattice surgeries in a gadget to the decoder, compute the value of the measurements, and send the measurement basis decision to the QPU is the first reaction time, labelled  $\gamma_{\text{LS}}$ . The second reaction time, labelled  $\gamma_{\text{mem}}$ , is the latency associated with the determining the measurement basis of the next correction qubit based on the measurement outcome of the previous correction qubit. Even though both these reactions are required for the same decision, they play a very different role in determining the schedule and speed of the computation. This is because the decoding of lattice surgeries in different gadgets can be parallelized, while the correction qubits must be decoded in sequence. Figure 3 illustrates the two reaction times in a sequence of rotation gadgets.

The lattice surgeries in different gadgets can be independently decoded by combining the two parallel window approaches. In both approaches, the reason for adding buffer regions to the windows is to reliably decode the commit region. However, the buffers are added only in either space or time dimensions. This means that in the space parallelization method, the initial temporal

boundaries of the windows must be specified, and usually these are determined by the decoding result of the directly preceding operation. If, however, temporal buffers are added at the start of each spatial window, then the lattice surgery can be decoded without knowledge of the decoding result of the previous operation. When this previous operation has finished decoding, it can commit these temporal buffers. To summarize, in our proposed approach, decoding a  $Y$  surgery will use windows of size

$$(x, z, t) = (2d, 2d, 2d), (2d, 1.5d, 2d), (d, d, 2d). \quad (4)$$

With this approach the lattice surgery decoding does not slow down the computation, and  $\gamma_{\text{LS}}$  only determines how long the correction qubit should be stored in memory before being measured. Note that the correction qubit is always stored in memory for one logical cycle during the  $PZ$  surgery, so its storage time is  $\gamma_{\text{LS}} + \tau_{\text{logical}}$ .

On the other hand, the decoding of the correction qubit measurement outcomes must be completed in sequential order. This is because, the decoding of the final two windows of the correction qubit before its measurement cannot be completed till the correction qubit is measured in some basis, and this basis is only decided once the previous correction qubit's measurement outcome has been completely decoded. In the core processor, if subsequent gadgets anti-commute, then they should not be executed faster than  $\gamma_{\text{mem}}$ , otherwise, the correction qubits will have to be placed in longer storage, waiting to be decoded in sequence. For utility-scale quantum computing, this storage could be billions or trillions of logical qubits in size, which is infeasible. Instead, the rate of execution of the rotation gadgets must be slowed down to match  $\gamma_{\text{mem}}$ . This requires storing the computational qubits in memory between the execution of two gadgets. Since, in any algorithm, the number of computational qubits is fixed (typically numbering in the hundreds or thousands), and space is already allocated to them, the choice of slowing down the computation only results in increased decoding resources. The number of decoding units needed in the core processor are computed in Section VI B. To summarize, a quantum circuit can be executed as fast as  $\gamma_{\text{mem}}T$ , where  $T$  is the number of rotation gadgets in the circuit. We assume this time-optimal case in this work.

In contrast to the core processor, the circuits executed in the MSF are typically very short. For example, each 15-to-1 magic state distillation unit requires the implementation of only 11 rotations [10]. These rotations can be performed sequentially every logical cycle time  $\tau_{\text{logical}}$ , producing one magic state every  $11\tau_{\text{logical}}$ . The freshly produced magic state must remain stored until all associated correction qubits have been measured. Since all operations in the 15-to-1 distillation protocol commute, if a sufficient number of classical processing units is available to decode all measurement outcomes in parallel, then the waiting time for the stored magic state is bounded by  $\gamma_{\text{mem}}$ . Therefore, the steady-state output rate of each distillation unit is one magic state every  $11\tau_{\text{logical}}$  given that the distillation process succeeds. This requires an additional storage area of  $\lceil \gamma_{\text{mem}}/\tau_{\text{logical}} \rceil$  patches in which both correction qubits and produced magic states are stored. This strategy is very advantageous because it prevents the multiplicative slowdown of magic state production when the MSF contains more than one level of distillation.

## V. REACTION TIME EFFECTS ON QUANTUM RESOURCE ESTIMATES

As discussed in the last section, for non-zero reaction time, the time-optimal run time of a quantum circuit is  $\gamma_{\text{mem}}T$ . However, the space cost has to be carefully calculated when optimizing the microarchitecture as described in Section II B. The reaction time has a number of effects on this optimization problem.

The state of computational qubits have to be protected in memory for  $\gamma_{\text{mem}}$ , which contributes to the accumulated logical error rate for the execution of the circuit. To remain within the target error budget, the code distance might have to be increased to reduce the error rate per memory protection operation. Also, the size of the correction qubit storage in the MSF increases proportionally with the reaction time, and they demand memory protection while stored, which may also require increasing the code distances used across distillation levels to keep accumulated logical error rates within the error budget. Finally, as reaction time increases, the rate at which magic states must be provided to the core processor decreases, resulting in a smaller MSF. This space trade-off is analyzed later in this section.

We compute a model for the error rates in a  $\pi/8$  gadget in Section V A. This model depends on the logical performance of quantum memory and lattice surgery. The performance of memory is presented in Section II C. In Section V B, we describe the simulations executed to estimate the performance of lattice surgery. These error rate models are used in the assembly of the microarchitectures. In Section V, we present our results on how the physical qubit count varies with the reaction time for two different quantum algorithms.

### A. Logical Error Rate Model for the Magic State Injection Gadget

We now describe how the two reaction times contribute to the logical error rate in the computation. To this end, we construct constitutive models for the logical error rates of the  $\pi/8$  rotation gadget. As the rotation involves fault-tolerant implementations of quantum memory and two lattice surgeries, we first present models for them. These logical error models are derived from the geometry of space-time diagrams of the quantum error correcting protocols, where the lengths and areas of various surfaces determine the coefficients in these models (see Fig. 8 of Ref. [3]).

For quantum memory on a square rotated surface code patch, the logical error rate is

$$P_{\text{mem}}(d, r) = \mu_S dr \Lambda_S^{-(d+1)/2}, \quad (5)$$

where  $d$  is the code distance and  $r$  is the number of syndrome measurement rounds, the latter of which we set to  $d$  in our microarchitecture [7, 13, 16, 32].

A lattice surgery typically involves multiple logical qubits connected by a bus. Suppose there are  $K$  logical qubits encoded in surface code patches of distance  $d$  and a bus consisting of  $B$  logical patches of distance  $d$ , and a lattice surgery of type  $Q = X^{\otimes K}$  is performed. Then, carefully accounting for the geometry of the space-time model associated with this lattice surgery, we obtain the following logical error rate model [1, 3, 13]:

$$P_{\text{LS}}(d, r, K, B) = \mu_X (K + B) dr \Lambda_X^{-(d+1)/2} + \mu_Z K d \Lambda_Z^{-(d+1)/2} + \mu_T B d^2 \Lambda_T^{-(r+1)/2}, \quad (6)$$

where  $r$  is the number of syndrome measurement rounds used in implementing the merging operations. The first term here accounts for logical  $X$  errors, which can occur anywhere on the logical qubits or the bus. However, logical  $Z$  errors can occur only on the logical qubits, and only just prior to merging or just after splitting. Hence, the second term has a smaller coefficient. The third term represents the time-like errors that can occur only on the bus patches and thus cause the value of the joint measurement to be incorrectly inferred. We assume an unbiased noise model, with identical error suppression for  $X$  and  $Z$  logical errors. Hence, we can set  $\mu_S = \mu_X = \mu_Z$  and  $\Lambda_S = \Lambda_X = \Lambda_Z$  and obtain the simplified expression

$$P_{\text{LS}}(d, r, K, B) = \mu_S [(K + B) dr + K d] \Lambda_S^{-(d+1)/2} + \mu_T B d^2 \Lambda_T^{-(r+1)/2}, \quad (7)$$

which due to symmetry between  $X$  and  $Z$  is applicable to lattice surgeries of any Pauli  $Q$ .

With these models in hand, we turn to the post-corrected  $\pi/8$  rotation. The first lattice surgery creates a two-qubit resource state. In our surface code architecture, the correction qubit is encoded in a rectangular code patch of dimensions  $d \times 2d$ . This allows  $Y$  lattice surgeries to be performed in a twist-based architecture [9]. A two-tile bus is needed to connect the  $Z$  logical operator of the magic state to the  $X$  and  $Z$  logical operators of the correction qubit. Hence, for this surgery,  $K = 3$  and  $B = 2$ . The second surgery that follows involves one of the qubits of the joint two-qubit resource state as well as  $K$  logical data qubits. For our simulations, we calculate the average number of logical data qubits  $K_{\text{avg}}$  in the compiled circuit, and estimate the average number of bus tiles  $B_{\text{avg}}$  used in each surgery. Hence, for this surgery,  $K = K_{\text{avg}} + 1$  and  $B = B_{\text{avg}}$ .

The reaction time  $\gamma_{\text{mem}}$  impacts the overall logical error rate of the  $\pi/8$  rotation because it results in a need for additional storage of qubits in quantum memory. The correction qubit is stored in memory for  $\gamma_{\text{LS}} + \tau_{\text{logical}}$  and the computational qubits are stored in memory for  $\gamma_{\text{mem}}$ , yielding

$$P_{\frac{\pi}{8}}(d) = P_{\text{LS}}(d, 3, 2) + P_{\text{LS}}(d, K_{\text{avg}} + 1, B_{\text{avg}}) + \frac{K\gamma_{\text{mem}} + \gamma_{\text{LS}} + \tau_{\text{logical}}}{\tau_{\text{logical}}} P_{\text{mem}}(d, d), \quad (8)$$

where the division by  $\tau_{\text{logical}}$  converts wall-clock time into a time expressed in terms of the number of logical cycles, because  $P_{\text{mem}}$  is the error of a single logical cycle. This model can be incorporated into the error budget used in our resource estimation analyses [3] discussed in Section V C. Before doing that, we estimate the performance of the lattice surgery protocol under our selected noise model.

## B. Lattice Surgery Error Rates

We estimate the performance of lattice surgery by numerically calculating the fitting parameters,  $\mu_S, \Lambda_S, \mu_T$  and  $\Lambda_T$  found in Eq. (7). We perform simulations in which two surface code patches of size  $d \times d$ , separated by one bus patch, also of size  $d \times d$  undergo a  $Q = XX$  lattice surgery. We perform two separate simulations to estimate the four fitting parameters.

In the first simulation, we determine  $\mu_S$  and  $\Lambda_S$  by setting  $r = d$  and varying  $d$ . First, the two computational qubit patches are prepared in  $|00\rangle_L$ , and the bus data qubits are prepared in  $|0\rangle$ . Next, a merged code is created by performing  $r$  merged stabilization rounds on the three patches. Then, the two codes are split by measuring the bus in the  $Z$  basis. The expected output state is  $(I + (-1)^m XX)|00\rangle_L = |00\rangle_L + (-1)^m |11\rangle_L$ , where  $m$  is the lattice surgery outcome. To validate this state, we measure all data qubits in the  $Z$  basis and determine the logical  $Z$  operator for the merged code,  $Z_{L,0} \otimes Z_{L,1} \otimes Z_{L,\text{bus}}$ . This operator is susceptible to logical  $X$  errors, but does not detect time-like failures. Hence, the leading-order term in Eq. (7) is

$$P_{\text{LS}}(d, d, 2, 1) \approx \mu_S \times 3d^2 \times \Lambda_S^{-\frac{d+1}{2}}. \quad (9)$$

In the second simulation, we determine  $\mu_T$  and  $\Lambda_T$  by setting  $d = 13$  and varying  $r$ . The computational qubit patches are prepared in  $|+0\rangle_L$ , which leads to the expected output state of

$$|+0\rangle_L + (-1)^m |+1\rangle_L = \begin{cases} |++\rangle & \text{if } m = 0, \\ |+-\rangle & \text{if } m = 1. \end{cases} \quad (10)$$

To validate this state, the data qubits of the second computational qubit are measured in the  $X$  basis, from which the value of the operator  $X_{L,1}$  can be inferred. While the value of this operator is random, its sum with  $m$  should be 0, unless a time-like error has flipped the value of  $m$ . Note that

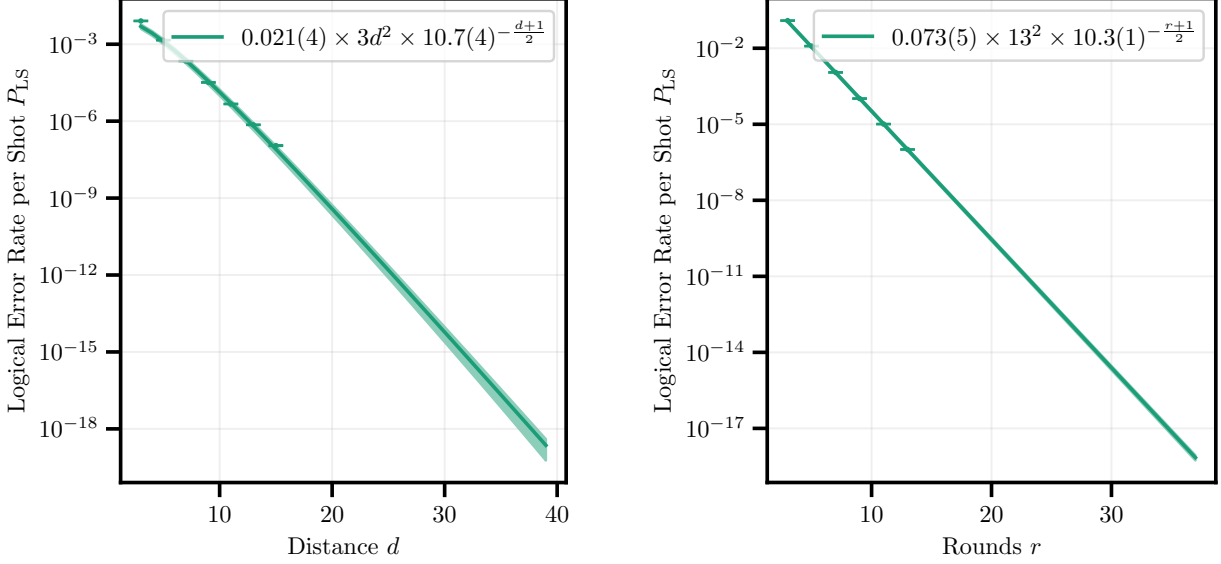


FIG. 4: Logical error rates of lattice surgery as a function of the distance  $d$  (left figure), and as a function of the number of rounds  $r$  (right figure). The simulations are performed using the error model from Ref. [1] in conjunction with the Target hardware parameter set specified in Table I. Data points are shown with error bars that have a range too small to be discernible. The data is fit to Eq. (9) and Eq. (11), respectively, and extrapolated to large distances. The uncertainties in the fits, depicted by the shaded regions, is small at the distances used in the assembled microarchitectures.

$X_{L,1}$  is sensitive to logical  $Z$  errors, which, however, have negligible probability in this simulation. Hence, the logical error rate is

$$P_{LS}(13, r, 2, 1) \approx \mu_T \times 13^2 \times \Lambda_T^{-\frac{r+1}{2}}. \quad (11)$$

The results of these simulations are shown in Fig. 4. The fitted parameter values are used in conjunction with Eq. (7) to determine the error rates of arbitrary lattice surgeries for the assembly process as described in the next section.

### C. Impact of Reaction Time on Physical Qubit Requirements

To illustrate how reaction time assumptions affect the space cost of a full fault-tolerant architecture, Fig. 5 shows the physical qubit count decomposed by architecture area (core processor, MSF distillation units, and MSF correction storage areas) as a function of the reaction time, assuming both memory and lattice surgery reaction times are equal. We plot estimates for two representative utility-scale circuits. The Fermi–Hubbard Plaquette Trotterization circuit [33] is characterized by a larger logical qubit count and a relatively lower  $T$  count, whereas the NMR spectral prediction for  $\alpha$ -conotoxin [34] represents the opposite regime, with a higher  $T$  count and fewer logical qubits. For both cases the data corresponds to time-optimal architectures on the space–time Pareto frontier. The trends in each curve reveal which areas of the architecture dominates the space overhead in different reaction time regimes.

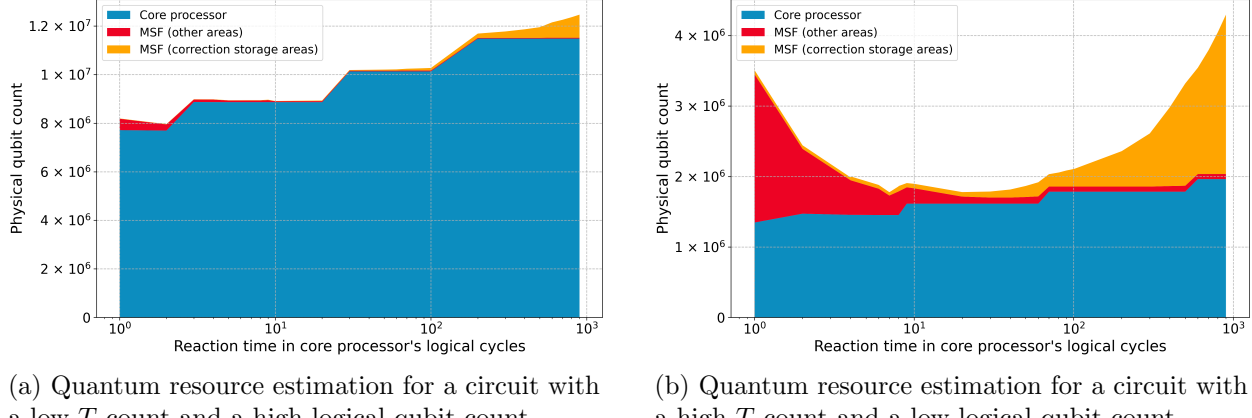


FIG. 5: Physical qubit footprint versus reaction time, measured in logical cycles of the core processor, broken down by architectural area. Estimates are provided for two contrasting utility-scale quantum algorithms: (a) ground-state energy estimation targeting a precision of 1.6 mHa for a 2D Fermi–Hubbard model on a  $32 \times 32$  lattice, using a circuit generated using Campbell’s Plaquette Trotterization approach [33], which requires 2562 logical qubits and  $4 \times 10^6 T$  gates; and (b) a single-shot dynamic-circuit implementation of the quantum eigenvalue transform for NMR spectral prediction of the  $\alpha$ -conotoxin macromolecule [34], requiring 241 logical qubits and  $5.11 \times 10^{11} T$  gates. For each algorithm, the figure shows the architecture chosen on the time-optimal branch of the space–time Pareto frontier generated using the TopQAD software suite [35].

We observe from the plots a clear trade-off between the red and yellow areas. Doubling the reaction time approximately halves the number of distillation units required in the MSF, thereby reducing the footprint of the MSF area used for distillation (red region). This occurs because a longer reaction time lowers the required magic state throughput.

However, each additional logical cycle of reaction time also requires one extra logical patch for correction qubit storage to buffer delayed decoding feedback. Consequently, doubling the reaction time doubles the storage overhead (yellow region). Within the utility-scale range tested, the MSF code distances vary from 23 in the single-level MSF for the shorter circuit (Fig. 5a) to 13 and 33 in the two-level MSF for the longer circuit (Fig. 5b). This results in an additional space overhead of roughly 1000–2500 physical qubits per extra logical cycle of reaction time. For the hardware model analyzed, this corresponds to an extra 100,000–250,000 physical qubits when decoder latencies are on the order of one millisecond, that is, 100 logical cycles of the core processor.

Another notable effect is the gradual growth of the core processor footprint with increasing reaction time. The code distance in the core must increase by one step for each reaction time increase of approximately a factor of  $\Lambda$  due to the extra memory protections. This trend is visible in our results for the  $\Lambda = 9.3$  hardware model, where each  $9.3 \times$  increase in reaction time triggers a code distance step-up. In the utility-scale range tested, core processor code distances range from 27 (shorter circuit) to 35 (longer circuit). A decoder latency of 100 logical cycles therefore raises these to 31 and 39, respectively, corresponding to additional physical qubit counts of 32% to 24%. For the circuits tested in the 200–2000 logical qubit range, this overhead corresponds to an additional approximately 300,000–1,750,000 physical qubits.

The dominant contributor to the total space cost depends on the circuit’s characteristics. For circuits requiring more computational qubits (see Fig. 5a), the core processor area dominates. In contrast, for circuits with a relatively higher  $T$  count (see Fig. 5b), the MSF area becomes the

Decoder	$\tau_d(N)$	Reference
Collision Cluster on FPGA (CC-FPGA)	$2.85 \times 10^{-10} N^{1.2}$	Fig. 4 in Ref. [23]
Collision Cluster on ASIC (CC-ASIC)	$5.53 \times 10^{-11} N^{1.34}$	Table 2 in Ref. [23]
AlphaQubit	$4.8 \times 10^{-6} N^{0.503}$	Extended Data Fig. 7 in Ref. [36]
PyMatching at $p = 0.1\%$	$5.91 \times 10^{-9} N^{1.17}$	Extended Data Fig. 7 in Ref. [36]

TABLE III: Decoding-time scaling for four surface code decoders. The values of  $\alpha$  and  $\beta$  in Eq. (12) for each decoder are numerically estimated by extracting data points from the indicated figures and table.

main driver of space cost. At short reaction times, the large number of parallel distillation units needed to sustain the required injection rate dominates the space overhead. At sufficiently large reaction times, correction storage patches becomes the dominant contributor.

These results show that developing faster decoders or communication links can decrease the distances required for utility-scale computations. Since decoding speed is typically a function of distance, this can set up a feedback loop of improvement. In the case of high  $T/Q$  circuits, decreasing the reaction time is counterproductive from a physical qubit count perspective. However, this can be alleviated by the development of either smaller magic state preparation units and distillation factory units, or ones with better error rates which can reduce the number of distillation levels required.

## VI. DECODER REQUIREMENTS

A key problem to solve in order to build utility-scale quantum computers is how fast individual decoding units need to be, and how many are needed. In Section VIA, we build a model for the reaction time, and use the model to analyze how fast decoding units need to be. In Section VIB, we estimate the number of decoders needed for a 10M qubit QPU.

### A. Speed

The reaction time is the sum of the decoding time and the communication latencies in the system, the latter of which have already been estimated in Section III A. The decoding time for a single decoding unit depends on the shape of the decoding graph passed to it, typically modelled as a linear function of the number of stabilization rounds  $r$ , but, as a monomial,

$$\tau_d(N) = \alpha N^\beta, \quad (12)$$

of the number of nodes  $N$  in the decoding graph. This model has been used to report the decoding speed of a number of decoders for a square memory patch of spatial size  $d^2$ , some of which are listed in Table III.

Using this model for the speed of a decoding unit, and recalling that temporal parallelization requires windows of size  $3d$ , the quantum memory reaction time is

$$\begin{aligned} \gamma_{\text{mem}} &= 3d\tau_d(d^2) + t_{\text{dd}} + 3d\tau_d(d^2) + t_{\text{qc}} + t_{\text{cd}} + t_{\text{do}} + t_{\text{oc}} + t_{\text{cq}} \\ &= 6d\tau_d(d^2) + t_{\text{dd}} + t_{\text{qc}} + t_{\text{cd}} + t_{\text{do}} + t_{\text{oc}} + t_{\text{cq}} \\ &= 6d\tau_d(d^2) + t_{\text{com}}, \end{aligned} \quad (13)$$

where the total communication time is

$$t_{\text{com}} = t_{\text{dd}} + t_{\text{qc}} + t_{\text{cd}} + t_{\text{do}} + t_{\text{oc}} + t_{\text{cq}}, \quad (14)$$

which is estimated to be  $t_{\text{com}} \approx 10 \mu\text{s}$  in Eq. (3). Many published quantum resource estimates assume a reaction time of  $10 \mu\text{s}$  [37–40] but our model shows that this budget is consumed by the communication latency alone. For comparison, using the window size from Eq. (4), the  $Y$ -type lattice surgery reaction time is

$$\begin{aligned} \gamma_{\text{LS}} &= 2d\tau_d(4d^2) + t_{\text{dd}} + 2d\tau_d(3d^2) + t_{\text{dd}} + 2d\tau_d(d^2) + t_{\text{qc}} + t_{\text{cd}} + t_{\text{do}} + t_{\text{oc}} + t_{\text{cq}} \\ &= 2d(4^\beta + 3^\beta + 1)\tau_d(d^2) + 2t_{\text{dd}} + t_{\text{qc}} + t_{\text{cd}} + t_{\text{do}} + t_{\text{oc}} + t_{\text{cq}}, \end{aligned} \quad (15)$$

with a slightly higher communication time due to the use of three layers of decoding.

The memory reaction time is related to the runtime  $t_{\text{circuit}}$  of a compiled quantum circuit with  $T$  magic state injections via

$$t_{\text{circuit}} = \gamma_{\text{mem}} T. \quad (16)$$

This equation and Eq. (13) can be combined to yield the speed of decoding a square memory patch

$$\tau_d(d^2) = \frac{t_{\text{circuit}}/T - t_{\text{com}}}{6d}. \quad (17)$$

Here,  $\tau_d(d^2)$  is the decoding speed per round of decoding a square memory patch of spatial size  $d^2$ . This enables a uniform comparison of the capabilities of different decoders.

Figure 6 plots, for  $d = 31$ , the decoding speed as a function of  $T$  for a few different  $t_{\text{circuit}}$ . It shows that, given a fixed circuit execution time, an improvement in decoding speed by an order of magnitude can yield improvements in the  $T$  count by roughly an order of magnitude. However, this advantage does not last forever because, as decoders become faster, the communication latency starts to dominate the reaction time. Another way for current or future decoders to become more powerful is if better compilation techniques were invented that reduce the  $T$  count of utility-scale algorithms. Yet another possible way to mitigate the impacts of large reaction times is to improve the physical error rates in the QPU. This is explored in Fig. 7, which plots, for  $T = 10^8$ , the decoding speed as a function of distance. Even though the two quantities are inversely related, halving the distance manages to improve decoding times by only about a third of an order of magnitude. The expected improvements in errors rates for superconducting qubits in the medium term will not result in such drastic improvements in the distance.

## B. Number and Size of Decoding Units

The minimal requirements for decoding space and time for a quantum computer are substantial, and the parallelization of lattice surgery decoding discussed in Section IV adds further costs. Therefore, we estimate the number and size of the decoding units required to keep up with the syndrome throughput. For simplicity, we restrict our analysis to the core processor, and ignore the MSF. In the core processor, only two logical operations occur. All computational qubits must be constantly stored in quantum memory, unless they are involved in the  $PZ$  lattice surgery of the rotation gadget, which happens every  $\lceil \gamma_{\text{mem}} / \tau_{\text{logical}} \rceil$  logical cycles. We make the worst-case assumption that the circuit has been compiled such that there is at least one multi-qubit operator  $P$  in the circuit that acts on all  $Q$  computational qubits and uses all  $B$  bus patches. Also note that in our architecture  $B \approx Q$ .

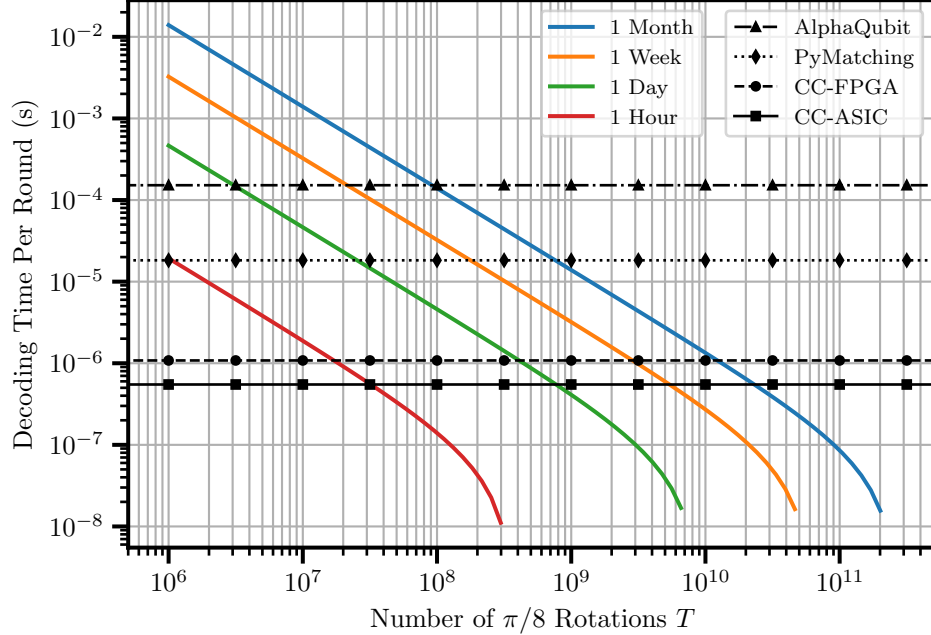


FIG. 6: Decoding speed of a square memory patch  $\tau(d^2)$  versus the number of magic state injections in a quantum circuit for a number of total circuit execution times, assuming that the core processor operates at  $d = 31$ . Also plotted are the decoding speeds of the decoders listed in Table III for  $d = 31$ . The fastest decoder (i.e., the CC-ASIC decoder) can execute circuits with  $T \leq 3 \times 10^7$  in an hour, and those with  $T \leq 2 \times 10^{10}$  in a month. Note that the communication latency  $t_{\text{com}}$  will begin to be a bottleneck below a decoding speed of  $10^{-7}$ .

When the computational qubits are in memory, the number of decoders required can be straightforward to estimate using an expression provided in Ref. [5], suitably modified for finite communication latency. The number of decoders required for a single patch is

$$k_{\text{mem}, 1} = \left\lceil \frac{2\tau_w + t_{\text{dd}}}{4\tau_{\text{logical}}} \right\rceil, \quad (18)$$

where  $\tau_w$  is the time needed to decode a single window. Since computational qubits are stored in pairs, the size of a window is  $(2d, d, 3d)$ , which yields  $t_w = 3d\tau_d(2d^2)$ . Hence, for  $Q$  logical qubits stored in pairs, the total number of decoders is

$$k_{\text{mem}} = \left\lceil \frac{Q[6d\tau_d(2d^2) + t_{\text{dd}}]}{8\tau_{\text{logical}}} \right\rceil, \quad (19)$$

each of which should be able to solve a problem of size  $(2d, d, 3d)$ .

For decoding a single lattice surgery, the parallelization algorithm has three layers, in each of which one-third of the cross-sectional area is committed. Hence, the number of parallel decoders needed is one-third of the number of patches in the surgery. According to our assumption above, there is a lattice surgery that involves  $Q + B \approx 2Q$  patches, which requires

$$k_{\text{LS}, 1} = \left\lceil \frac{2Q}{3} \right\rceil \quad (20)$$

parallel decoders. The first layer involves the largest problems of size  $(2d, 2d, 2d)$  (see Eq. (4)), which sets the minimum size for the decoding units. As discussed in Section IV, lattice surgery

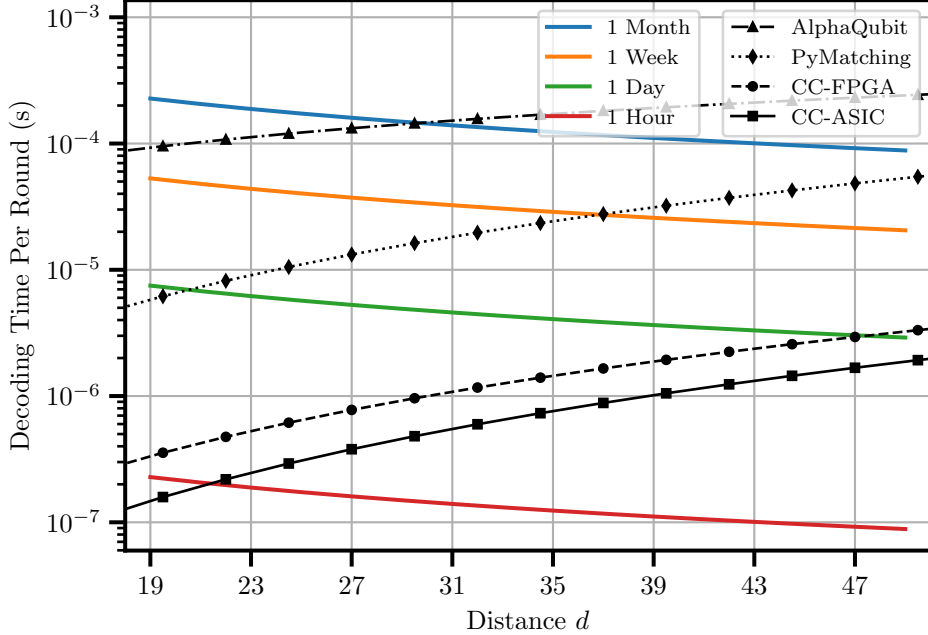


FIG. 7: Decoding speed of a square memory patch  $\tau(d^2)$  versus the distance of the core processor for a number of total circuit execution times, assuming a circuit  $T$  count of  $10^8$ . Also plotted as a function of distance are the decoding speeds of the decoders listed in Table III. The decoding speed is not very sensitive to the distance at this  $T$  count.

decoding can be parallelized, and  $\lceil \gamma_{\text{LS}}/\gamma_{\text{mem}} \rceil$  such decodings can occur in parallel. For the two Collision Cluster decoders listed in Table III, this factor is 4. Hence, for the lattice surgery decoding, we estimate that

$$k_{\text{LS}} = \left\lceil \frac{8Q}{3} \right\rceil \quad (21)$$

parallel decoders are needed.

As  $\gamma_{\text{LS}} > \gamma_{\text{mem}}$ , both the memory and lattice surgery decoding tasks are happening in parallel; hence, the total number of decoding units needed is

$$k = \left\lceil \frac{Q[6d\tau_d(2d^2) + t_{\text{dd}}]}{8\tau_{\text{logical}}} \right\rceil + \left\lceil \frac{8Q}{3} \right\rceil. \quad (22)$$

We estimate this number assuming we have a core processor that operates at  $d = 31$  and occupies 90% of a 10-million-qubit QPU, the CC-ASIC decoding model is used, and  $t_{\text{dd}} = 0.5 \mu\text{s}$  (see Table II). This results in  $k \approx 13,200$ . Adding a 10% additional cost for the MSF, we estimate that the decoder cluster will need about  $\sim 15,000$  decoding units, which is a fairly substantial cost. This number can potentially be improved with alternate codes, more-efficient FTQC architectures, or improved decoder parallelization algorithms.

We conclude this section by computing the maximum memory required for storing the syndromes in the decoder cluster's memory. The syndromes associated with the lattice surgery must be stored in the decoder cluster's memory for  $2d(4^\beta + 3^\beta + 1)\tau_d(d^2) + 2t_{\text{dd}}$  (see Eq. (15)). Assuming that all 5 million syndrome qubits in a 10-million-qubit QPU are stored for this long, the memory required is  $\sim 1800 \text{ MB}$ . This is an overestimate because the syndromes of each layer can be discarded as soon as the associated decoding tasks are complete, and an underestimate because it ignores the lattice surgery parallelization overhead.

## VII. CONCLUSION

In this paper, we have presented the results of our analysis of the performance of a quantum computer with respect to the speed of decoding units and the latencies of the classical control electronics. Since our microarchitecture relies on post-corrected magic state injection, the reaction time associated with quantum memories (pertaining to correction qubits of the injection gadget) are the main bottlenecks for the speed of quantum computation. Based on this insight, we built a model for the additional logical error that is accumulated while the qubits are idling between subsequent magic state injections. Using this model, we assembled the quantum circuits for execution in our FTQC microarchitecture and determined the physical qubit count as a function of the reaction time. We conducted quantitative numerical studies for two different applications based on two different quantum algorithms: ground-state energy estimation of a 2D Fermi–Hubbard model based on quantum phase estimation using Campbell’s Plaquette Trotterization approach [33]; and NMR spectral prediction for a macromolecule based on the quantum eigenvalue transform [34]. These studies gave rise to the following three key insights. First, improving the reaction time by a factor of two allows for doubling the size of the magic state factories because magic states can be consumed faster in the core processor. Second, the same factor-of-two improvement in the reaction time also halves the space required to store the correction qubits in the magic state factories. Third, a decrease in reaction time by a factor of  $\Lambda$  (which is the error suppression factor for quantum memory) results in a decrease in the distance of the code by 2. Our results highlight the tradeoff between the size of the quantum processor and its physical error rates, given a fixed decoding speed.

We also designed a system architecture for the quantum execution environment of the computer, and experimentally estimated the latencies of transferring information between its components. We combined these communication latencies with the decoding speed of parallel space- and time-window decoders to build models for the reaction times. Our estimates of reaction times are much greater than the  $10\text{ }\mu\text{s}$  figure typically assumed in the literature. Using the reaction time models, we established, given a fixed circuit execution time, the tradeoff curves between decoder speed and both the  $T$  count and the distance of the code. Our results show that the fastest decoders currently available will need weeks or months to execute utility-scale quantum circuits. However, we found that an order of magnitude improvement in decoding speed can make circuits with an order of magnitude higher  $T$  count accessible in the same execution time. Finally, we estimated that the execution environment of a 10M-qubit computer will require a thousand-channel high-speed communication link between the orchestrator, controller, and decoder cluster, with the decoder cluster consisting of  $\sim 15\text{k}$  nodes, each capable of decoding independent patches of distance  $\sim 30\text{--}60$ .

The intention of our work was to ascertain the magnitude of the improvements needed in decoding speeds and communication electronics, as well as other aspects of a quantum computer, to make FTQC a reality. Our results suggest that decoders or control electronics need to be significantly faster than they currently are to execute useful circuits. However, improved compilation to reduce the  $T$  count of algorithms or improved error rates to reduce the distance of the core processor can also expand the utility landscape. Another promising avenue for future development is the design of codes with better rates and distances than the surface code. Our results also show that methods of magic state preparation and distillation with lower space cost or error rates can significantly reduce the total physical qubit count.

## ACKNOWLEDGEMENTS

We thank our editor, Marko Bucyk, for reviewing the manuscript, and Alan Ho and John Martinis for useful conversations. The authors acknowledge the financial support of Pacific Economic Development Canada (PacifiCan) under project number PC0008525, and DARPA’s Quantum Benchmarking Initiative (QBI) under project number HR0011-25-9-0116. G. A. D. is grateful for the support of Mitacs. P. R. acknowledges the financial support of Innovation, Science and Economic Development Canada (ISED), the Province of Ontario through the Ministry of Colleges and Universities, and the Perimeter Institute for Theoretical Physics.

---

[1] Masoud Mohseni, Artur Scherer, K Grace Johnson, Oded Wertheim, Matthew Otten, Navid Anjum Aadit, Yuri Alexeev, Kirk M Bresnicker, Kerem Y Camsari, Barbara Chapman, et al. How to Build a Quantum Supercomputer: Scaling from Hundreds to Millions of Qubits, 2024. URL <https://arxiv.org/abs/2411.10406>.

[2] Craig Gidney and Austin G. Fowler. Flexible layout of surface code computations using AutoCCZ states, 2019. URL <https://arxiv.org/abs/1905.08916>.

[3] Allyson Silva, Artur Scherer, Zak Webb, Abdullah Khalid, Bohdan Kulchytskyy, Mia Kramer, Kevin Nguyen, Xiangzhou Kong, Gebremedhin A. Dagnew, Yumeng Wang, Huy Anh Nguyen, Einar Gabassov, Katiemarie Olfert, and Pooya Ronagh. Optimizing Multi-level Magic State Factories for Fault-Tolerant Quantum Architectures, 2024. URL <https://arxiv.org/abs/2411.04270>.

[4] Sophia Fuhui Lin, Eric C. Peterson, Krishanu Sankar, and Prasahnt Sivarajah. Spatially parallel decoding for multi-qubit lattice surgery. *Quantum Sci. Technol.*, 10(3):035007, 2025. doi:10.1088/2058-9565/adc6b6.

[5] Luka Skoric, Dan E. Browne, Kenton M. Barnes, Neil I. Gillespie, and Earl T. Campbell. Parallel window decoding enables scalable fault tolerant quantum computation. *Nat. Commun.*, 14(1):7040, 2023. doi:10.1038/s41467-023-42482-1.

[6] Eric Dennis, Alexei Kitaev, Andrew Landahl, and John Preskill. Topological quantum memory. *J. Math. Phys.*, 43(9):4452–4505, 2002. doi:10.1063/1.1499754.

[7] Austin G. Fowler, Matteo Mariantoni, John M. Martinis, and Andrew N. Cleland. Surface codes: Towards practical large-scale quantum computation. *Phys. Rev. A*, 86(3):032324, 2012. doi:10.1103/PhysRevA.86.032324.

[8] Dominic Horsman, Austin G. Fowler, Simon Devitt, and Rodney Van Meter. Surface code quantum computing by lattice surgery. *New J. Phys.*, 14(12):123011, 2012. doi:10.1088/1367-2630/14/12/123011.

[9] Daniel Litinski and Felix von Oppen. Lattice Surgery with a Twist: Simplifying Clifford Gates of Surface Codes. *Quantum*, 2:62, 2018. doi:10.22331/q-2018-05-04-62.

[10] Daniel Litinski. A Game of Surface Codes: Large-Scale Quantum Computing with Lattice Surgery. *Quantum*, 3:128, 2019. doi:10.22331/q-2019-03-05-128.

[11] Austin G. Fowler and Craig Gidney. Low overhead quantum computation using lattice surgery, 2018. URL <https://arxiv.org/abs/1808.06709>.

[12] Alexander Erhard, Hendrik Poulsen Nautrup, Michael Meth, Lukas Postler, Roman Stricker, Martin Ringbauer, Philipp Schindler, Hans J. Briegel, Rainer Blatt, Nicolai Friis, and Thomas Monz. Entangling logical qubits with lattice surgery. *Nature*, 589(7841):220–224, 2021. doi:10.1038/s41586-020-03079-6.

[13] Christopher Chamberland and Earl T. Campbell. Universal Quantum Computing with Twist-Free and Temporally Encoded Lattice Surgery. *PRX Quantum*, 3(1):010331, 2022. doi:10.1103/PRXQuantum.3.010331.

[14] Austin G. Fowler. Time-optimal quantum computation, 2012. URL <https://arxiv.org/abs/1210.4626>.

[15] Kevin C Miao, Matt McEwen, Juan Atalaya, Dvir Kafri, Leonid P Pryadko, Andreas Bengtsson, Alex Opremcak, Kevin J Satzinger, Zijun Chen, Paul V Klimov, et al. Overcoming leakage in quantum error correction. *Nature Physics*, 19(12):1780–1786, 2023. doi:10.1038/s41567-023-02226-w.

- [16] Google Quantum AI and Collaborators. Quantum error correction below the surface code threshold. *Nature*, 638(8052):920–926, 2025. doi:10.1038/s41586-024-08449-y.
- [17] Craig Gidney, Noah Shutty, and Cody Jones. Magic state cultivation: growing T states as cheap as CNOT gates, 2024. URL <https://arxiv.org/abs/2409.17595>.
- [18] F Battistel, C Chamberland, K Johar, R W J Overwater, F Sebastian, L Skoric, Y Ueno, and M Usman. Real-time decoding for fault-tolerant quantum computing: Progress, challenges and outlook. *Nano Futures*, 7(3):032003, 2023. doi:10.1088/2399-1984/aceba6.
- [19] Antonio deMarti iOlius, Patricio Fuentes, Román Orús, Pedro M. Crespo, and Josu Etxezarreta Martínez. Decoding algorithms for surface codes. *Quantum*, 8:1498, 2024. doi:10.22331/q-2024-10-10-1498.
- [20] Barbara M. Terhal. Quantum error correction for quantum memories. *Rev. Mod. Phys.*, 87:307–346, 2015. doi:10.1103/RevModPhys.87.307.
- [21] Nicolas Delfosse and Naomi H. Nickerson. Almost-linear time decoding algorithm for topological codes. *Quantum*, 5:595, 2021. doi:10.22331/q-2021-12-02-595.
- [22] Poulam Das, Christopher A. Pattison, Srilatha Manne, Douglas M. Carmean, Krysta M. Svore, Moinuddin Qureshi, and Nicolas Delfosse. Afs: Accurate, fast, and scalable error-decoding for fault-tolerant quantum computers. In *2022 IEEE International Symposium on High-Performance Computer Architecture (HPCA)*, pages 259–273, Seoul, Korea, Republic of, 2022. IEEE. ISBN 978-1-6654-2027-3. doi:10.1109/HPCA53966.2022.00027.
- [23] Ben Barber, Kenton M. Barnes, Tomasz Bialas, Okan Buğdayci, Earl T. Campbell, Neil I. Gillespie, Kauser Johar, Ram Rajan, Adam W. Richardson, Luka Skoric, Canberk Topal, Mark L. Turner, and Abbas B. Ziad. A real-time, scalable, fast and resource-efficient decoder for a quantum computer. *Nat. Electron.*, 8(1):84–91, 2025. doi:10.1038/s41928-024-01319-5.
- [24] Héctor Bombín, Chris Dawson, Ye-Hua Liu, Naomi Nickerson, Fernando Pastawski, and Sam Roberts. Modular decoding: Parallelizable real-time decoding for quantum computers, 2023. URL <https://arxiv.org/abs/2303.04846>.
- [25] Xinyu Tan, Fang Zhang, Rui Chao, Yaoyun Shi, and Jianxin Chen. Scalable surface-code decoders with parallelization in time. *PRX Quantum*, 4(4):040344, 2023. doi:10.1103/PRXQuantum.4.040344.
- [26] Tim Chan. Snowflake: A distributed streaming decoder, 2024. URL <https://arxiv.org/abs/2406.01701>.
- [27] Kai Zhang, Jubo Xu, Fang Zhang, Linghang Kong, Zhengfeng Ji, and Jianxin Chen. Latte: A decoding architecture for quantum computing with temporal and spatial scalability, 2025. URL <https://arxiv.org/abs/2509.03954>.
- [28] Craig Gidney. Stim: A fast stabilizer circuit simulator. *Quantum*, 5:497, 2021. doi:10.22331/q-2021-07-06-497.
- [29] Oscar Higgott. PyMatching: A Python package for decoding quantum codes with minimum-weight perfect matching, 2021. URL <https://arxiv.org/abs/2105.13082>.
- [30] Yue Wu, Namitha Liyanage, and Lin Zhong. An interpretation of union-find decoder on weighted graphs, 2022. URL <https://arxiv.org/abs/2211.03288>.
- [31] Peter-Jan H. S. Derkx, Alex Townsend-Teague, Ansgar G. Burchards, and Jens Eisert. Designing fault-tolerant circuits using detector error models, 2024. URL <https://arxiv.org/abs/2407.13826>.
- [32] J. Kelly, R. Barends, A. G. Fowler, A. Megrant, E. Jeffrey, T. C. White, D. Sank, J. Y. Mutus, B. Campbell, Yu Chen, Z. Chen, B. Chiaro, A. Dunsworth, I.-C. Hoi, C. Neill, P. J. J. O’Malley, C. Quintana, P. Roushan, A. Vainsencher, J. Wenner, A. N. Cleland, and John M. Martinis. State preservation by repetitive error detection in a superconducting quantum circuit. *Nature*, 519(7541):66–69, 2015. doi:10.1038/nature14270.
- [33] Earl T. Campbell. Early fault-tolerant simulations of the Hubbard model. *Quantum Sci. Technol.*, 7(1):015007, 2021. doi:10.1088/2058-9565/ac3110.
- [34] Justin E. Elenewski, Christina M. Camara, and Amir Kalev. Prospects for NMR Spectral Prediction on Fault-Tolerant Quantum Computers, 2024. URL <https://arxiv.org/abs/2406.09340>.
- [35] 1QB Information Technologies (1QBit). TopQAD: Topological Quantum Architecture Design [Software Documentation]. 2024. doi:10.70781/YPWW8761.
- [36] Johannes Bausch, Andrew W Senior, Francisco JH Heras, Thomas Edlich, Alex Davies, Michael Newman, Cody Jones, Kevin Satzinger, Murphy Yuezhen Niu, Sam Blackwell, et al. Learning high-accuracy error decoding for quantum processors. *Nature*, 635(8040):834–840, 2024. doi:10.1038/s41586-024-08148-8.

- [37] Craig Gidney and Martin Ekerå. How to factor 2048 bit rsa integers in 8 hours using 20 million noisy qubits. *Quantum*, 5:433, 2021. URL <http://arxiv.org/abs/1905.09749>.
- [38] Joonho Lee, Dominic W. Berry, Craig Gidney, William J. Huggins, Jarrod R. McClean, Nathan Wiebe, and Ryan Babbush. Even more efficient quantum computations of chemistry through tensor hypercontraction. *PRX Quantum*, 2(3):030305, 2021. doi:10.1103/PRXQuantum.2.030305.
- [39] Daniel Litinski and Naomi Nickerson. Active volume: An architecture for efficient fault-tolerant quantum computers with limited non-local connections, 2022. URL <http://arxiv.org/abs/2211.15465>.
- [40] Craig Gidney. How to factor 2048 bit RSA integers with less than a million noisy qubits, 2025. URL <https://arxiv.org/abs/2505.15917>.